Yield estimation of the 2020 Beirut explosion using open access waveform and remote sensing data

Christoph Pilger[1,*], Peter Gaebler[1], Patrick Hupe[1], Andre C. Kalia[1], Felix Schneider[2], Andreas Steinberg[1], Henriette Sudhaus[3], and Lars Ceranna[1]

[1]Federal Institute for Geosciences and Natural Resources (BGR), 30655 Hannover, Germany
[2]GFZ German Research Centre for Geosciences, 14473 Potsdam, Germany
[3]Christian Albrechts University, 24118 Kiel, Germany
[*]Corresponding author: christoph.pilger@bgr.de

ABSTRACT

We report on a multi-technique analysis using publicly available data for investigating the huge, accidental explosion that struck the city of Beirut, Lebanon, on August 4, 2020. Its devastating shock wave led to thousands of injured with more than two hundred fatalities and caused immense damage to buildings and infrastructure. Our combined analysis of seismological, hydroacoustic, infrasonic and radar remote sensing data allows us to characterize the source as well as to estimate the explosive yield. The latter ranges between 0.8 and 1.1 kt TNT (kilotons of trinitrotoluene) equivalent and is plausible given the reported 2.75 kt of ammonium nitrate as explosive source. As there are strict limitations for an on-site analysis of this catastrophic explosion, our presented approach based on data from open accessible global station networks and satellite missions is of high scientific and social relevance that furthermore is transferable to other explosions.

Introduction

The explosion that occurred in the city of Beirut, Lebanon, on the 4th of August 2020 around 18:08 local time (15:08 UTC) was caused by the combustion of approximately 2.75 kt of ammonium nitrate stored in a harbour warehouse, as announced by the government shortly afterwards. This accidental event led to thousands of injured with more than two hundred fatalities[1]. An enormous shock wave following the explosion caused immense damage to buildings and infrastructure, also shattering windows all over the city. On-site investigations into the cause and nature of the explosion are conducted by local authorities[2]. Nevertheless, the access to the site of an explosion can be limited due to various reasons. It can e.g. be harmful to go near the explosion site, when chemicals or radioactivity pollute the area. This means that direct information and data can be sparse or there is a need for an independent validation. For the explosion in Beirut there were some of those limitations in place for on-site investigations, also due to its timing in a high-time of the SARS-CoV-2 pandemic. So for significant explosions with a large impact on people, like in the case of Beirut, transparent investigations that use open methods to analyse explosions reliably, based on publicly available data, are important. We therefore offer an independent, third-party estimation of the yield of the explosion from the analysis of publicly available waveform and remote sensing data.

During the last 100 years a number of anthropogenic explosions occurred which were remotely detected by seismic or acoustic sensors. The first one reported in the context of acoustic propagation and perception happened in 1921 at a BASF plant in Oppau, Germany[3], also originating from the combustion of ammonium nitrate. The seismoacoustic imprint of many following man-made explosions was recorded during the era of nuclear testing (1945 to 1998)[4] until opening for signature of the Comprehensive Nuclear-Test-Ban Treaty (CTBT)[5]. In later years, only the Democratic People's Republic of Korea performed (underground) nuclear tests, which were consistently detected by CTBT's International Monitoring System (IMS) and other seismic and infrasonic stations as well as satellite remote sensing[6,7].

The IMS as well as other seismic and infrasonic networks recorded a large number of further accidental explosions during the 21th century[8–11]. Albeit the catastrophic nature and aftermath of many of these explosions happening in or near inhabited areas, such events provide valuable datasets for remote sensing and propagation studies as well as monitoring and verification issues. The sub-audible sound waves of the Beirut explosion propagated through the atmosphere to distances of thousands of kilometers and were recorded by infrasound arrays of the IMS. Seismic, hydroacoustic and acoustic signals propagated through solid earth, water and air and were recorded at nearby land-based and ocean-bottom seismometers. We assess damages to buildings in the city with spaceborne synthetic aperture radar (SAR) imagery from before and after the explosion and link damage maps with overpressure caused by the explosion. Here we analyse this combined dataset within the present study to benchmark origin time and epicentre of the event. We focus on a consistent yield estimate based on results from the different methods.

Waves from the explosion traveling through Earth, ocean and atmosphere

We inspected publicly available data from seismometers located in the region around Beirut. Multiple signals in distances of up to 400 km have been detected (see Fig. 1a), where energy propagated as seismic, hydroacoustic and acoustic waves through ground, ocean and atmosphere, respectively. The map in Fig. 1b shows the spatial distribution of the stations color coded by the dominant phase detected.

On seismometers north and south of Beirut the seismic phases are dominant. These have been observed on the majority of the inspected stations. Due to the location of the explosion in the harbour of Beirut, part of the energy has also been released directly into the water, which caused the hydroacoustic signal to be the dominant phase on all ocean bottom seismometers (stations IM.CY*), located in the eastern Mediterranean Sea south of Cyprus. Moreover, by hydroacoustic-to-seismic coupling this signal was also clearly recorded on island stations located near the coast of Cyprus (CQ.MVOU and KO.EREN).

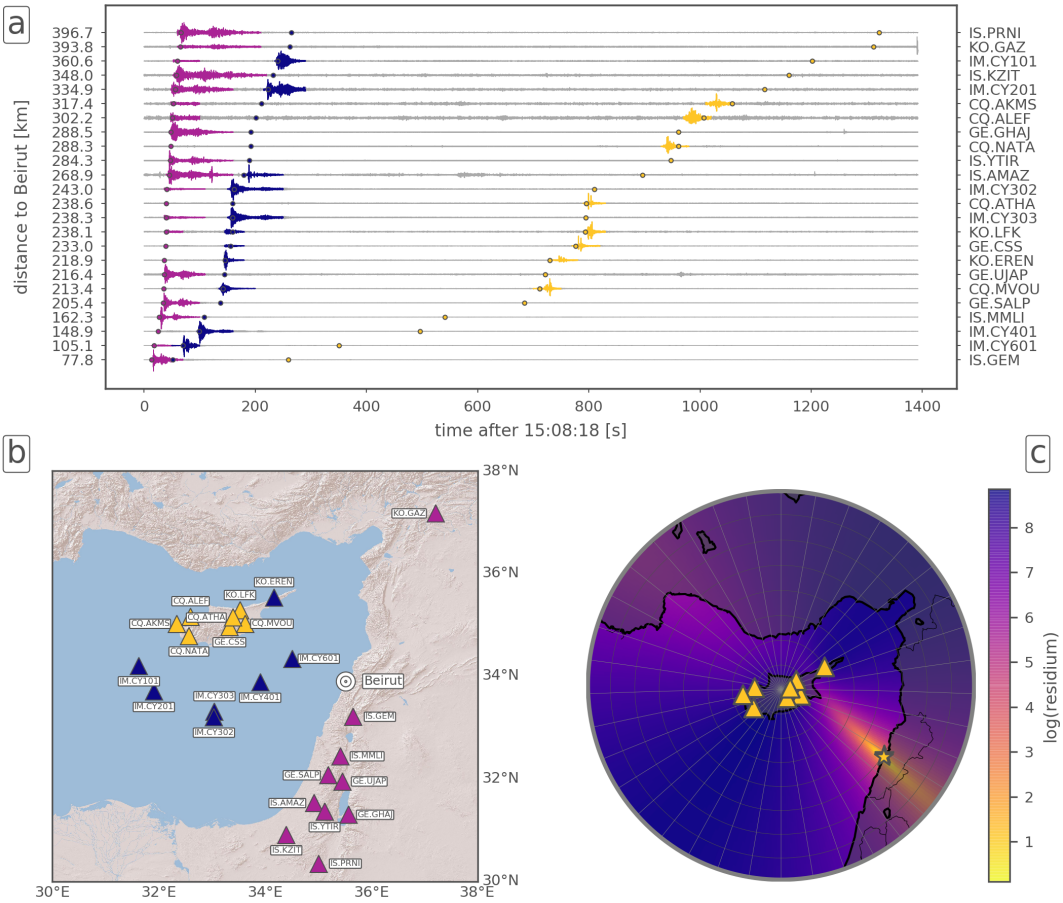

Figure 1. Data from regional seismic stations. (a) Waveforms of the seismic stations. Colored circles (purple, blue, yellow) represent theoretical arrivals of phases propagating with seismic (6.0 km/s), hydroacoustic (1.5 km/s) or acoustic (0.3 km/s) velocities. Observed waveform arrivals of seismic, hydroacoustic or acoustic phases are color coded in the respective colors. Waveforms are bandpass-filtered in the frequency band 0.5 to 8.0 Hz. (b) Seismic stations with distances of up to 400 km from the explosion site in Beirut. Station colors represent the type of the dominant observed phase (seismic = purple, hydroacoustic = blue, acoustic = yellow), see also subfigure (a). (c) Localization procedure for the acoustic phase detected on the eight seismic stations located on the island of Cyprus (see Met. M.1 for details). Color coded is a residuum, which defines the optimal localization at its smallest value. The best location is found at 33.863°N, 35.502°E, marked as yellow star close to Beirut.

All stations located on Cyprus furthermore detected acoustic signals that have been coupled into the ground by acoustic-to-seismic coupling[12], as observed also at other large explosions[10]. Infrasound most efficiently propagates from the source to receivers in a stratospheric waveguide[13], in which the signal energy is continuously reflected between the surface and the upper stratosphere while the damping is low. This waveguide evolves if the along-path wind speed in about 50 km is sufficiently

high such that the effective sound speed equals or exceeds the sound speed at the ground; i. e. the effective sound speed ratio ($v_{\mathrm{eff-ratio}}$) equals or exceeds one. In the summer, the easterly stratospheric winds favor infrasound detections in western direction. Using the seismoacoustic phases from seismic stations on Cyprus, we localized the origin of the explosion. The yellow star in Fig. 1c marks the best location, which we found at 4.8 km south of the harbour of Beirut. Our localization technique confirms the acoustic nature of the signals (apparent velocity of 344 m/s) as well as the source origin (see Met. M.1 for details).

We invert the observed regional broadband seismic waveforms recorded in distances up to 400 km to characterize the explosion in terms of onset time, duration and strength. Also our ability to well locate the explosion is tested here, even though the location is known. For representing the explosion we use force couples in form of a moment tensor (Met. M.2). Our estimates give an onset time for the explosion of 15:08:18.63 UTC, a duration of 2.9 s and a location at 33.91°N, 35.52°E. The moment tensor representation is estimated to relate to a seismic moment magnitude M_w 3.47. We can now relate the seismic moment via the shear stress change to the energy of the explosion (Met. M.3.1), which results in a yield estimate of 1.08 kt.

We apply an additional method to estimate the yield of the explosion from seismic data. This approach relies on the relation of teleseismic body wave magnitude m_b measurements to the seismic yield of an explosion (Met. M.3.2) and results in an estimate of 0.13 to 0.3 kt TNT for the explosion. These values have to be considered a lower bound estimate, as the relations are established for well-coupled underground nuclear explosions. For a surface explosion only a small portion of the total energy couples into the subsurface[14] as seismic energy and is subsequently considered in the m_b measurements.

Infrasonic signatures observed at thousands of kilometers distance

We analyse data from IMS infrasound arrays in distances up to 10,000 km to identify signatures potentially related to the Beirut explosion. We apply the progressive multi-channel correlation (PMCC) method[15] (see Met. M.4). Obtained back-azimuth information from the different arrays allows localization, and we use peak-to-peak amplitudes as well as dominant periods for yield estimation.

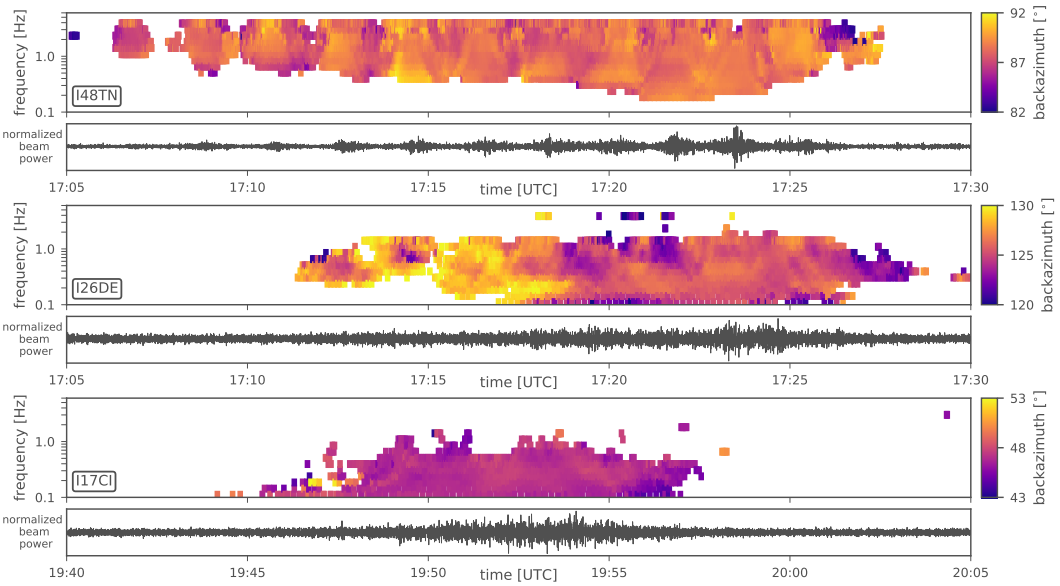

Figure 2. Infrasound analyses for the three stations I48TN in Tunisia, I26DE in Germany and I17CI in Ivory Coast using the PMCC method. Top frames show color-coded back-azimuth information of each time-frequency-pixel in a 10° segment centered around the true direction towards Beirut. Bottom frames show corresponding waveform beams of differential pressure, bandpass-filtered between 0.5 and 8.0 Hz.

The array analysis yields detections associated with the explosion at five IMS infrasound stations (see Tab. A1): I48TN (Tunisia), I26DE (Germany), I17CI (Ivory Coast), I42PT (Azores) and I11CV (Cape Verde Islands). We focus on I48TN, I26DE and I17CI as these exhibit the highest signal content (see Tab. A1) and thus lower parameter uncertainty. Fig. 2 shows their PMCC analyses. A remarkable feature visible in the station recordings is the signal separation into various pressure pulses

at I48TN. These pulses are related to the separation of signal energy of one single blast into multiple stratospheric propagation paths from the source to the receiver, as was also observed for the Buncefield explosion in 2005[8].

Fig. 3 shows the IMS infrasound stations detecting the Beirut explosion as well as the propagation conditions depicted by $v_{\mathrm{eff-ratio}}$ (a) and the localization results (b). The source location (see Met. M.4) that we determine using five IMS stations is 56 km south (33.4334°N, 35.3067°E) of the actual origin; whereas we improve the localization (33.5067°N, 35.4666°E) to only 44 km south of the actual origin when we use only the three best detecting stations. Given the large station distances, this result proves the capability of the IMS infrasound network for event localization.

We estimate the explosive yield based on data of the three infrasound arrays I48TN, I26DE and I17CI. We apply the AFTAC and LANL relations (see Met. M.4), the latter one using both climatological (HWM14) and numerical weather forecast (ECMWF) models. The input parameters and resulting yields are summarized in Tab. A2 with final explosive yield estimates derived by averaging over the three stations.

We find that the AFTAC and LANL (HWM14) relations correspond very well with resulting maximum yields of 1.1 kt TNT. Although the AFTAC relation is primarily used for explosive sources at higher altitude like meteors[16] and is independent of the actual ducting conditions, it is applicable here because we only consider stations within good stratospheric ducting conditions. When we account for more precise ECMWF profiles in the LANL relation we estimate a yield of about 0.5 kt TNT. However, the empirical LANL relation is based on wind speeds derived from climatologies. Therefore, precise ECMWF profiles seem to be less appropriate for estimating yields with the LANL relation and will not be considered any further.

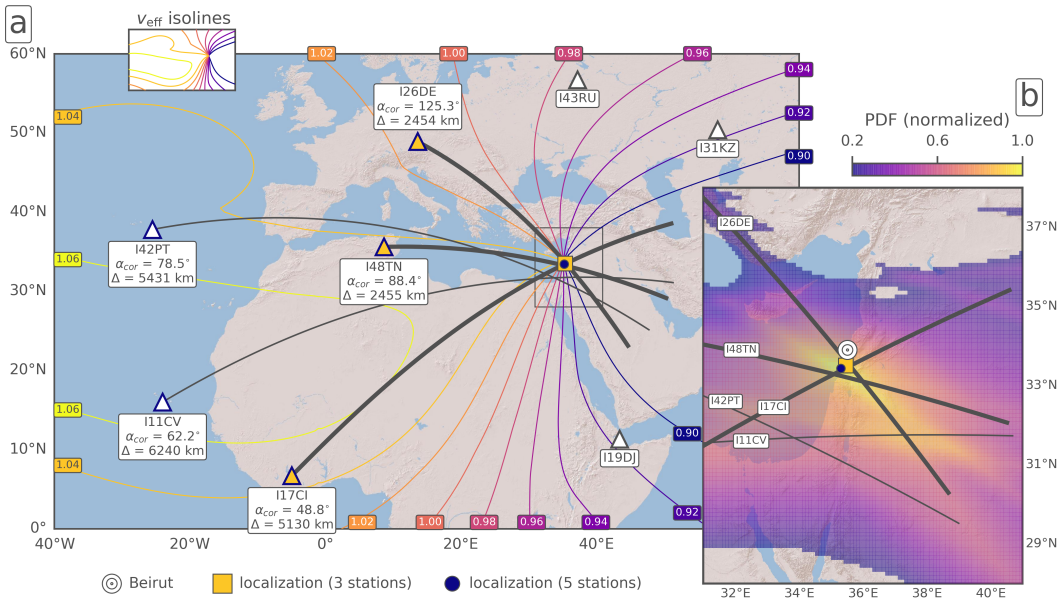

Figure 3. Localization of the explosion using IMS infrasound data. (a) IMS stations (triangles) and effective sound speed ratio ($v_{\mathrm{eff-ratio}}$) isolines respective to the source location, based on the HWM14 model for 16:00 UTC. The great-circle projections (black lines) correspond to the ECMWF-corrected PMCC back-azimuths (α_{cor}) of the detecting stations. The stations with the highest signal content – given in Fig. 2 and used for yield estimation – are highlighted (yellow triangle, thick lines). IMS stations at which $v_{\mathrm{eff-ratio}} < 0.98$ did not detect the explosion due to the prevailing easterly stratospheric winds. (b) Details of the localization using the grid-search approach (see Met. M.4). The maximum of the normalized probability density function (PDF) depicts the optimum location of the grid-search approach using the five detecting stations. It results in a deviation of 56 km to the southwest (blue circle) of the actual origin (white circle). Relying on the three best-detecting stations results in a slightly improved location at 44 km to the south (yellow square) as the back-azimuth uncertainty is smaller.

Linking overpressure simulations and InSAR derived damage maps

The blast of the explosion caused a wide range of damages to buildings. The reflection of radar waves from SAR satellites are strongly depending on the ground structure down to a decimeter level, with a sensitivity to less than a centimeter of motion. In areas of Beirut, where the outsides of buildings have been significantly damaged, space-borne SAR images that show the

backscattered amplitude and phase of radar waves before and after the explosion therefore differ. To quantify this difference and thereby the building damage, we use a combined measure of the amplitude and phase similarity in multitemporal SAR image pixels, the interferometric coherence, which we relate to relative damage (Fig. 4a, Met. M.5). We then calculate the explosive yield necessary to produce such damage. Most damage of an explosion is caused by the produced overpressure. The empirical relation "BOOM"[17] developed from conventional explosive tests between 0.1 and 1 kt of TNT is used to relate the yield of an explosive to its resulting peak overpressure P (in Pa) at any given distance r (in m) for a surface explosion (Met. M.6). We assume a relation between peak overpressure and resulting damage[18]. We set 80 kPa peak overpressure to result in 100% damage to all structures. We further assume that due to dampening in urban areas damage scales with distance. We use ground-truth available from media reports (Fig. A3 and Tab. A4) to calibrate between the relative damage values from the damage pixels and the relative damage from peak overpressure. We evaluate the developed relation at the distances between the explosion and mapped damage pixels from InSAR data and solve for the necessary yield in TNT to cause the observed damage. The resulting yield estimations are shown in Fig. 4b. Maximum observed damage values are well bound by the damage estimate of a yield of 1.1 kt TNT. The best fitting yield is calculated by us to be 0.8 kt TNT (shown as damage circles in Fig. 4a), which results in a minimization of differences between inferred damage and predicted damage, especially in the near-field (< 500 m distance from the explosion).

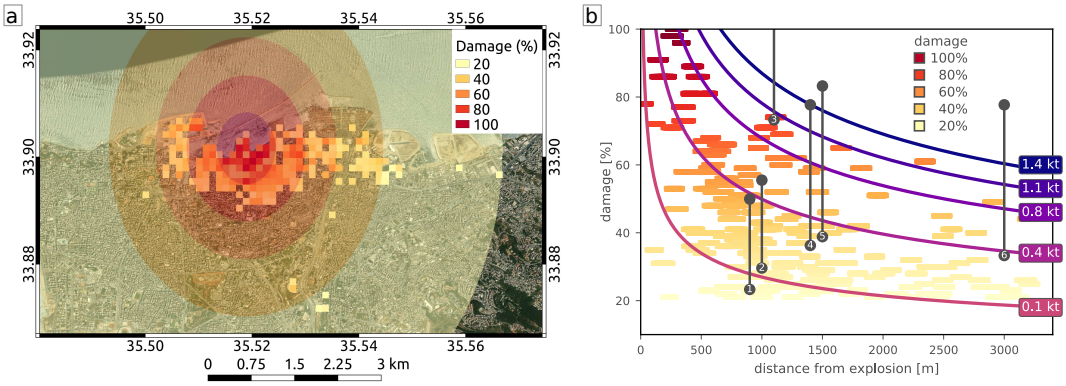

Figure 4. Yield estimation through comparison of inferred and estimated expected damage over distance from the explosion site. a) Relative damage and expected damage map over an optical satellite image background (Sentinel-2). Shown is the relative damage pixel map as colored pixels. The damage is measured in percent of pixels that experienced significant loss of interferometric coherence after the explosion in a windowed damage pixel of 100 m by 100 m size. The transparent overlay indicates the radii of the expected damage from a yield of 0.8 kt TNT and is colored after the relative damage classes[18]. b) Measured damage and expected damage for several evaluated yields over distance from the explosion site. Eq. 3 is evaluated for yields of 0.1, 0.4, 0.8, 1.1 and 1.4 kt of TNT at the distances of the damage pixels and plotted as lines. Measured damage is plotted as in a). Numbered vertical lines relate to reported and here damage-classified locations (see Fig. A3) used for calibration.

Discussion

The Beirut 2020 explosion coupled into ground, water and air and accordingly generated seismic, hydroacoustic and infrasonic wave signatures observed and analysed within this study. We inferred the temporal and spatial source characteristics using seismic and acoustic methods, resulting in a location accuracy of 44 km using remote IMS infrasound arrays and below 1 km when using regional seismic stations. Combining the IMS infrasound detections with near-field observations of acoustic phases potentially improves the location accuracy.

All three independent methods that we apply (seismic moment tensor inversion, acoustic yield relations, satellite radar image analysis) consistently estimate the range of the yield to be between 0.8 and 1.1 kt TNT equivalent. Taking into account the fact that ammonium nitrate has an explosive efficiency of about 50% of TNT and that most but not all of the energy of the explosion was released into the atmosphere in terms of a devastating shock wave, the resulting yield estimates are consistent with the announced amount of 2.75 kt of ammonium nitrate being the source of the explosion.

We developed a novel approach to infer the yield of an explosion from the damage measured as changes in radar satellite remote sensing images from before and after the explosion. Most damage to structures due to an explosion is caused by overpressure.

Each explosive yield results in a specific overpressure level at given distances. This allows us to estimate the yield of the explosion by relating the expected radius and expected damage to the observed damage from radar satellite remote sensing images. This approach is operationally feasible because of the unique Sentinel-1 mission characteristics. They include the long-term mission design, a continuous acquisition plan of the Earth´s surface with high frequency and a free, full and open data policy.

Considering the design goal of the IMS infrasound network, we were able to reliably identify, locate and characterize an atmospheric (surface) explosion with a yield around 1 kt TNT with three or more stations. Nevertheless, improvements of the location accuracy and an independent mean to confirm the origin and yield of an explosion can be provided by considering freely available seismometer and spaceborne remote sensing data as national technical means to the monitoring and verification capabilities of the CTBT.

Methods

M.1 Seismoacoustic localization procedure for stations located in Cyprus

We performed a grid-search to localize the origin of the acoustic signals detected on the seismometers in Cyprus. Fig. 1c shows the result for distances ranging from 0 to 400 km and back-azimuths ranging from 0° to 360°with distance and back-azimuth spacings of 2 km and 1°, respectively, with respect to the center location of the seismometers. For each location, we performed a linear regression analysis in order to find the apparent velocity fitting the observed seismoacoustic arrivals best. The logarithm of the residuum of the least-squares solution is color coded in Fig. 1c. The lowest residuum is found at (33.863°N, 35.502°E), which is located 4.8 km south of the harbour of Beirut, marked as yellow star. In order to define the arrival times, the z-components of each station were selected in a time window of $\pm$400 s with respect to an expected arrival time, assuming a celerity of 0.3 km/s. Waveforms were bandpass-filtered between 0.5 Hz and 4 Hz and normalized to their maximum amplitudes. In order to get rid of waveform variations due to different atmospheric paths we used smoothed envelopes of the traces and defined the maximum of the smoothed envelopes as arrival time. Smoothing was done by a zero-phase Butterworth lowpass filter with a corner period of 10 s. Fig. A1 shows the original seismic traces (gray), the smoothed envelopes and the resulting straight line (red dashed line), which fits best the arrival times at the location with the minimum residuum. The vertical offsets of the traces are proportional to the distance of the respective stations from the best location. Note that the resulting velocities are not absolute velocities (celerities) but an average trace velocity across the array. Thus the resulting velocity cannot be used to infer the origin time. However, by assuming an average celerity of 0.3 km/s, the origin time can be inferred from the best location as 15:08:13.4 UTC $\pm$ 6 s, which is in agreement with the ground truth time of 15:08:18 UTC.

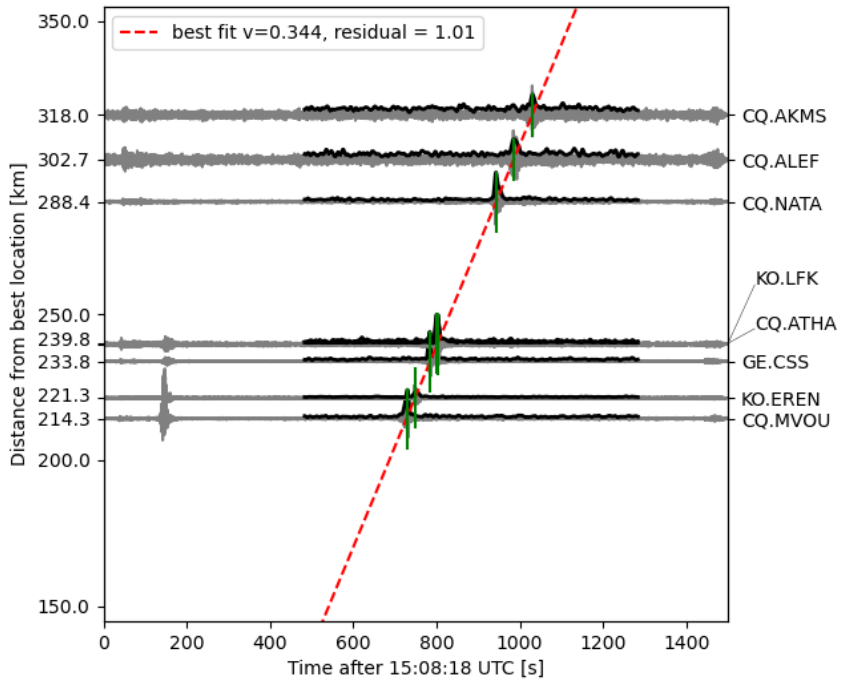

Figure A1. Seismoacoustic localization procedure for seismic stations located in Cyprus. The figure shows continuous waveforms (grey) and their smoothed envelopes (black) in the selected time window. The maxima of the latter were used to define the arrival times (marked as green lines). During grid-search, for each location the least-squares solution is derived, that best fits a straight line through the arrival times. Here, the case of the lowest residuum is shown, which is achieved for an apparent velocity $v = 0.344$ km/s at the location (33.863°N, 35.502°E) (see yellow star in Fig. 1c).

M.2 Explosion source inversion

We carry out an inversion of regional broadband seismic waveforms up to 400 km distance to infer source parameters. We assume an isotropic explosion source with the source parameters location (lat, lon), time, duration, depth and magnitude. We fix the depth at the surface. We allow the location to vary around 1 km from the known location of the blast. We use the "Grond" optimization algorithm[19]. Synthetic waveforms are calculated using a 20 Hz Green's function store using the QSEIS code by Wang (1999)[20] and based on a composite 1-D velocity model[21,22]. We downsample the waveform records to 20 Hz and filter with a Butterworth bandpass of fourth order between 1.2 Hz and 3 Hz. We compare synthetics and data in a tapered window between 0.5 s before and after the theoretical P-wave onset for the closest station and between 0.5 s before and 2.5 s for all other stations. To compensate for unmodeled 3-D path effects we allow at each station an individual shift of the trace of up to 1 s to maximize fit. We assign the closest station manually double the weight in comparison to other stations. We make the results available online as a report under https://www.seismologie.bgr.de/sdac/erdbeben/big_quakes/beirut_report/index.html#/. We find the best fitting source parameters to be a magnitude of 3.47 (seismic moment of 1.8×10^{14} N m) with a source duration of 2.9 s and an onset time of source time to be 15:08:18.63 UTC and the origin location to be 33.9050°N and 35.5185°E.

M.3 Yield estimation from seismic data

Two methods are applied to estimate the yield of the explosion using seismic data.
(1) The first method to estimate the yield of the explosion relies on the relation of seismic moment and strain energy drop via the shear stress change $\Delta\sigma$ and shear modulus μ[23]:

$$E = \frac{\Delta\sigma}{2\mu} M_0 \tag{1}$$

Evaluating Eq. 2 for a yield of 1.1 kt TNT very close to the source (0.01 m distance) leads to roughly 10^8 Pa stress change. Assuming the seismic moment M_0 of 1.8×10^{14} Nm determined in Section M.2 and the 2×10^9 Pa shear modulus based on the used velocity model results in a yield estimate of 1.08 kt TNT. This approach implicitly assumes the yield for estimating the shear stress change from Eq. 2. This nevertheless validates the consistency between Eq. 2 and the determined seismic moment. We note that the empirical relations and assumptions of Eq. 2 are probably invalid very close to the source and that the choice of the distance evaluated strongly impacts the resulting yield estimate. Relations between energy and seismic moment are not straightforward and the assumption is taken that the shear stress change can be estimated at first order from the pressure change, which neglects other energy conversion contributions during an explosion.
(2) The second method of yield estimation applied here relies on the relation of seismic body wave magnitude (m_b) measurements to the yield of an explosion. This relation is commonly and widely used in the field of nuclear underground test monitoring, but might also be used to provide a lower bound of an explosive source on the surface. The relation between m_b and yield depends on multiple factors, such as the geological setting at the source site, the efficiency of wave propagation from source to receiver, the depth of the explosion, as well as the coupling of the source to the underground. Due to these factors it is not possible to state one single relation, but rather empirical relations developed for different areas are required. These empirical formulas are of the type $m_b = A + B\log(Y)$, where Y is the seismic yield of the explosion in kt TNT equivalent and A and B are constants depending on the aforementioned factors. These empirical equations have been used in different regions for calibration, for example at the Nevada test site[24] ($Y = 3.92 + 0.81\log(Y)$), in Kazakhstan[25] ($Y = 4.45 + 0.75\log(Y)$) or in Nova Zemlya[26] ($4.25 + 0.75\log(Y)$). As these relations only hold true for well coupled underground explosions, seismic coupling factors for above ground explosions given by Bornmann et al. (2009)[14] have to be taken into account. The International Data Center (IDC) of the CTBT organization states a body wave magnitude (m_b) of 3.2 for the Beirut explosion in its Reviewed Event Bulletin. This value for m_b can be related to seismic yield in kt TNT equivalent of the explosion. According to Brax et al. (2016)[27] the geological unit at the explosion site is comprised out of dolomite rocks and the region can be classified as International Building Code (IBC) class C (very dense soil and soft rock). Under these geological assumptions we use m_b yield relations for wet hard rock[24] and for dry unconsolidated rock[7] to estimate a range of explosive yield of the explosions. These relations result in a yield estimate of 0.13 to 0.34 kt TNT equivalent for the explosion. For surface explosions only a small portion of the total released energy couples into the subsurface as seismic energy. According to Bornmann et al. (2009)[14] seismic coupling factors for a surface explosion can be as low as 0.1% and therefore our yield assessment based on m_b relations has to be considered as a lower bound estimate.

M.4 Infrasound array analysis, location and yield estimation

IMS infrasound array data within this study are analysed using the progressive multi-channel correlation (PMCC) method[15] available from the DTK-GPMCC application in the National Data Center (NDC)-in-a-Box package. The main objective of the NDC-in-a-Box project and the interactive array processing tool DTK-GPMCC is to offer the capability of processing and analysing IMS waveform data to all NDCs of CTBT member states. PMCC is applied to the raw differential pressure recordings at each of the IMS infrasound arrays' microbarometers to derive advanced data parameters like back-azimuth, apparent velocity and frequency content of coherent signals associated with different events. Back-azimuth reflects the horizontal direction of signal origin, while apparent velocity indicates the arrival inclination, where higher values correspond to propagation from higher-altitude ducts. Signals are identified as pixel information in distinct time steps and frequency bands, and they are clustered to signal families related to the same event. The third-octave band configuration with an inverse frequency-distributed window length is implemented[28].

For quantifying the explosive yield using PMCC data, two different acoustic methods are established: The AFTAC relation (Air Force Technical Application Center)[16] solely depends on the dominant signal period at maximum amplitude. The LANL relation (Los Alamos National Laboratory)[29] depends on source-to-receiver distances and wind-corrected amplitude measurements, thus also incorporating climatological or real-time stratospheric wind profiles.

The source localization using the IMS infrasound network is based on a grid-search algorithm[8,30]. It relies on both the detected back-azimuths and the arrival times at the stations. The grid covers the map shown in Fig. 3 with a resolution of 0.1°. The detected back-azimuths are corrected by the atmospheric propagation conditions using the method applied by Pilger et al. (2018)[31], which also provides a celerity estimate. For each grid point, the residuals of the corrected back-azimuths are computed and linearly weighted (the weight is one if the residual is zero, and zero if the residual is larger than the back-azimuth tolerance of 1° (for three stations) or 5° (for five stations). Also, the differential travel times of all two-station combinations are computed for each grid point and linearly weighted (the time tolerance is 90 s). The sum of the weighted functions results in a two-dimensional probabilistic density function (PDF), the maximum of which is the optimum location of the grid-search algorithm.

Atmospheric profiles are assembled from high-resolution analysis fields (up to around 75 km) provided by the European Centre for Medium-Range Weather Forecasts (ECMWF) and the Horizontal Wind Model as of 2014 (HWM14)[32].

The PMCC method was applied to all IMS stations within 10,000 km distance. Signal parameters from five IMS infrasound arrays that could be associated to the Beirut explosion are provided in Tab. A1. Visualisation of the PMCC results for the three stations I48TN, I26DE and I17CI are provided in Fig. 2. Follow-up analyses of source localization and yield estimation using these PMCC results are provided in Fig. 3 and Tab. A2.

Table A1. Parameters of the Beirut explosion signatures as derived from PMCC analysis of different IMS arrays.

parameter	I48TN	I26DE	I17CI	I42PT	I11CV
distance [km]	2455	2454	5130	5431	6240
back-azimuth [°]	88.4	126.3	47.2	77.9	60.7
apparent speed [m/s]	357	350	341	341	355
mean frequency [Hz]	2.57	0.71	0.37	0.66	0.84
number of pixels [#]	7544	2840	944	62	58
signal start [UTC]	17:06:17	17:11:19	19:44:06	20:20:42	20:44:56
signal end [UTC]	17:27:34	17:28:46	19:57:35	20:24:02	20:56:17

Table A2. Parameters and results for infrasound-based yield estimation using different IMS arrays and methods

parameter	I48TN	I26DE	I17CI	resulting yield average
dominant period at maximum amplitude [s]	4.6	4.6	5.4	
maximum peak-to-peak amplitude [Pa]	0.48	0.12	0.13	
stratospheric wind (HWM14) [m/s]	26.8	19.7	8.0	
stratospheric wind (ECMWF) [m/s]	48.6	24.6	18.4	
yield for AFTAC method [kt TNT]	0.86	0.86	1.47	1.06
yield for LANL (+HWM14) method [kt TNT]	0.91	0.22	2.02	1.05
yield for LANL (+ECMWF) method [kt TNT]	0.25	0.17	1.10	0.51

M.5 InSAR damage maps

Two ascending and two descending track's of Sentinel-1 interferometric wide swath data pairs are used for the coherence change detection (CCD). For each track the acquisitions take place at different times and the radar waves also have different incident angles. Therefore, they sense the damage on the ground independently and from different observation geometries. Each

Table A3. Details of the Sentinel-1 data used in the study. Data are acquired in interferometric wide swath mode by Terrain Observation with Progressive Scans (TOPS) in vertical/vertical (VV) polarization. The single look complex SAR images were downloaded from the Copernicus Open Access Hub.

		pre-explosion		co-explosion	
heading	rel. orbit	primary	secondary	primary	secondary
ascending	87	29.07.2020	23.07.2020	04.08.2020	29.07.2020
ascending	14	30.07.2020	24.07.2020	05.08.2020	30.07.2020
descending	94	30.07.2020	24.07.2020	05.08.2020	30.07.2020
descending	21	31.07.2020	25.07.2020	06.08.2020	31.07.2020

track's dataset consists of two acquisitions from before the explosion (pre-explosion) and a pair of acquisitions from before and after the explosion (co-explosion; see Tab. A3). The enhanced spectral diversity algorithm[33] is used to precisely coregister the Sentinel-1 acquisition pairs on a burst level. Subsequently, the coherence is estimated for each acquisition pair using a 5 by 5 pixel window and an adaptive filter[34]. The coherence is a correlation coefficient of the complex SAR signal and ranges between 0 and 1. The results are geocoded and consist of eight coherence maps from four different acquisition geometries (two ascending and two descending). For each track we perform a CCD independently by subtracting the co-explosion coherence from the pre-explosion coherence (Fig. A2). The coherence loss of a single pixel is caused by e. g. damaged buildings or additive noise caused by a bias of the coherence estimator. By assuming that a coherence loss of $\geq$0.2 indicates damage, we create a binary representation of the coherence loss in form of damage and no-damage pixels. In order to increase the accuracy of the damage estimation, the four independent CCD maps are combined. If damage is indicated in at least one CCD map (CCD$\geq$0.2), we assign damage also in the combined binary damage image. How strongly an area is damaged is finally evaluated based on the percentage of damage pixels in a 10 by 10 pixel window (roughly 100 by 100 m), which forms the damage map (Fig. 4a).

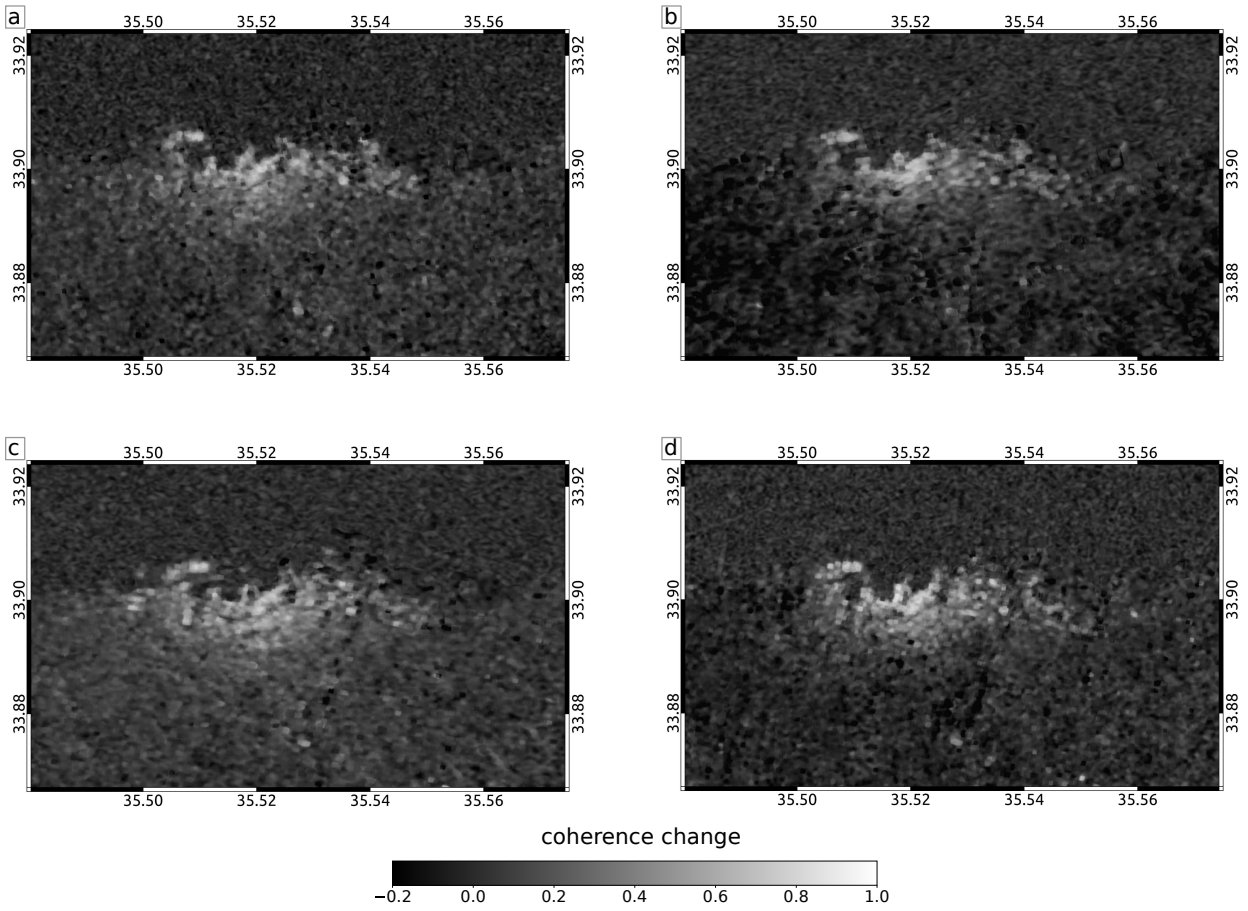

Figure A2. Sentinel-1 coherence change detection results for relative orbit 87 (a), 14 (b), 95 (c) and 21 (d).

M.6 Yield estimation from InSAR damage maps

We link the InSAR observation to the yield via peak overpressure calculations, which give an expected level of damage for a certain yield at a given distance. We use the empirical relation "BOOM"[17] for conventional explosive tests between 0.1 and 1 kt of TNT that relates the yield of an explosive to its resulting peak overpressure P (in Pa) at any given distance r (in m) for a surface explosion:

$$P = \frac{3.45978 \times 10^6 \cdot w^{0.444} \cdot A^{0.556}}{r^{1.333}} \tag{2}$$

A is the atmospheric pressure (1006 hPa, ECMWF data between 12 and 18 UTC) and w is the yield of the explosion in kt TNT equivalent.
We assume a relationship between damage and peak overpressure[18] and we set 80 kPa peak overpressure to result in 100% damage to all structures. Due to dampening of the shock wave in urban areas from structures we expect that damage scales with distance. Ground-truth (Fig. A3a and Tab. A4) is used to calibrate between the relative damage values from the damage pixels and the expected damage from peak overpressure:

$$D = P \cdot 3.7\mathrm{e}^{-3} \cdot r. \tag{3}$$

The above equation is evaluated at the distances between the explosion and mapped damage pixels from InSAR data and solved for the necessary yield in TNT to cause the observed damage.

Table A4. Ground-truth used for calibration of the relation between relative damage inferred from InSAR data and damage caused by peak overpressure. See map of locations in Fig. A3. For each location the distance is given relative to explosion location and damage levels are estimated from available media coverage and reports. The related peak overpressure is derived based on the reported damage after [18, table B-2].

number	locality	distance	est. damage	est. overpressure (kPA)
1	Sursock Palace	0.9 km	partial demolition - partial collapse roof	7-15
2	Saint George hospital	1 km	minor damage, partial demolition	8-15
3	Seaside Arena	1.1 km	serious structural damage, collapse	18-40
4	Saint George church	1.4 km	minor damage	7-15
5	Forum de Beyrout	1.5 km	metal buckled	7–15
6	Hotel Cavalier	3 km	minor damage, buckling	3–7

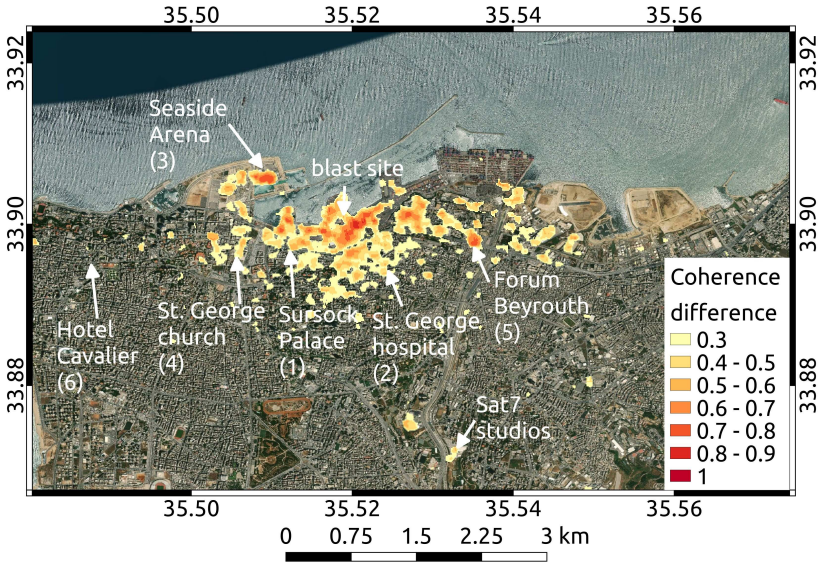

Figure A3. Coherence loss map. Shown is the coherence difference from all combined InSAR scenes. The color indicates the coherence difference, describing the coherence loss between scenes before and after the explosion. Coherence differences <0.3 are masked. Arrows point at notable locations and sites used as ground-truth (Tab. A3) as reference for calibration of Eq. 3.

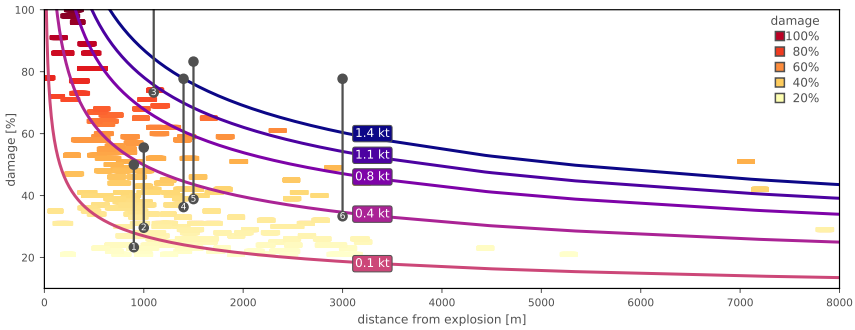

Figure A4. Yield estimation through comparison of measured and estimated expected damage over distance up to 3500 m from the explosion site. The damage is measured in percent of pixels that experienced significant coherence loss after the explosion in a windowed damage pixel of 100 m by 100 m size (Fig. A3) and plotted from light (less damage) to hot colors (more damage). Eq. 3 is evaluated for yields of 0.1, 0.4, 0.8, 1.1 and 1.4 kt of TNT at the distances of the damage pixels and plotted as lines. Numbered black bar plots indicate ground-truth based damage estimations used for calibration from numbered locations in Fig. A3. A yield of 1.1 kt TNT bounds most maximal damage observed and the near-field damage is best explained by a yield of 0.8 kt TNT.

References

1. Guglielmi, G. Why Beirut's ammonium nitrate blast was so devastating. *Nature.* DOI: 10.1038/d41586-020-02361-x (2020).
2. Abdalmohsen, R. 'You can't imagine the disaster we're living in': Lebanon's researchers struggle to cope with explosion aftermath. *Nature.* DOI: 10.1038/d41586-020-02437-8 (2020).
3. Gutenberg, B. Über die ausbreitung des schalles in der atmosphäre. *Naturwissenschaften* **14**, 338–342 (1926).
4. Stevens, J., Divnov, I., Adams, D., Murphy, J. & Bourchik, V. Constraints on infrasound scaling and attenuation relations from soviet explosion data. In *Monitoring the Comprehensive Nuclear-Test-Ban Treaty: Data Processing and Infrasound*, 1045–1062 (Springer, 2002).
5. Dahlman, O., Mykkeltveit, S. & Haak, H. *Nuclear test ban: converting political visions to reality* (Springer Science & Business Media, 2009).
6. Pilger, C., Ceranna, L. & Bönnemann, C. *Monitoring Compliance with the Comprehensive Nuclear-Test-Ban Treaty (CTBT)* (Schweizerbart'sche Verlagsbuchhandlung, 2017).
7. Gaebler, P. *et al.* A multi-technology analysis of the 2017 north korean nuclear test. *Solid Earth* **10**, 59–78 (2019).
8. Ceranna, L., Le Pichon, A., Green, D. & Mialle, P. The buncefield explosion: a benchmark for infrasound analysis across central europe. *Geophys. J. Int.* **177**, 491–508 (2009).
9. Green, D. N., Vergoz, J., Gibson, R., Le Pichon, A. & Ceranna, L. Infrasound radiated by the gerdec and chelopechene explosions: Propagation along unexpected paths. *Geophys. J. Int.* **185**, 890–910 (2011).
10. Schneider, F. M. *et al.* Seismo-acoustic signals of the baumgarten (austria) gas explosion detected by the alparray seismic network. *Earth Planet. Sci. Lett.* **502**, 104–114 (2018).
11. Fuchs, F., Schneider, F. M., Kolínskỳ, P., Serafin, S. & Bokelmann, G. Rich observations of local and regional infrasound phases made by the alparray seismic network after refinery explosion. *Sci. reports* **9**, 1–14 (2019).
12. Novoselov, A., Fuchs, F. & Bokelmann, G. Acoustic-to-seismic ground coupling: coupling efficiency and inferring near-surface properties. *Geophys. J. Int.* **223**, 144–160, DOI: 10.1093/gji/ggaa304 (2020).
13. Drob, D. P., Picone, J. M. & Garcés, M. Global morphology of infrasound propagation. *J. Geophys. Res. Atmospheres* **108**, 4680, DOI: 10.1029/2002JD003307 (2003).
14. Bormann, P. *et al.* *New Manual of Seismological Observatory Practice (NMSOP)*, chap. Seismic Sources and Source Parameters, 1–102 (Deutsches GeoForschungsZentrum GFZ, 2009).
15. Cansi, Y. An automatic seismic event processing for detection and location: The pmcc method. *Geophys. research letters* **22**, 1021–1024 (1995).
16. ReVelle, D. O. Historical detection of atmospheric impacts by large bolides using acoustic-gravity waves. *Annals New York Acad. Sci.* **822**, 284–302 (1997).
17. Douglas, D. A. Blast operational overpressure model (boom): An airblast prediction method. Tech. Rep., AIR FORCE WEAPONS LAB KIRTLAND AFB NM (1987).
18. CCPS. *Guidelines for evaluating the characteristics of vapor cloud explosions, flash fires, and BLEVEs* (Center for Chemical Process Safety of the American Institute of Chemical, 1994).
19. Heimann, S. *et al.* Grond: A probabilistic earthquake source inversion framework. (2018).
20. Wang, R. A Simple Orthonormalization Method for Stable and Efficient Computation of Green's Functions. *Bull. Seismol. Soc. Am.* **89**, 733–741 (1999).
21. Di Luccio, F. & Pasyanos, M. Crustal and upper-mantle structure in the eastern mediterranean from the analysis of surface wave dispersion curves. *Geophys. J. Int.* **169**, 1139–1152 (2007).
22. Bassin, C. The current limits of resolution for surface wave tomography in north america. *EOS Trans. AGU. 81: Fall Meet. Suppl., Abstr.* (2000).
23. Kanamori, H. The energy release in great earthquakes. *J. Geophys. Res.* **82**, 2981–2987 (1977).
24. Murphy, J. R. *Identification of Seismic Sources — Earthquake or Underground Explosion*, chap. P Wave Coupling of Underground Explosions in Various Geologic Media, 1201–205 (Springer Netherlands, Dordrecht, 1981).
25. Ringdal, F., Marshall, P. D. & Alewine, R. W. Seismic yield determination of Soviet underground nuclear explosions at the Shagan River test site. *Geophys. J. Int.* **109**, 65–77, DOI: 10.1111/j.1365-246X.1992.tb00079.x (1992).

26. Bowers, D., Marshall, P. D. & Douglas, A. The level of deterrence provided by data from the SPITS seismometer array to possible violations of the Comprehensive Test Ban in the Novaya Zemlya region. *Geophys. J. Int.* **146**, 425–438, DOI: 10.1046/j.1365-246x.2001.01462.x (2001).

27. Brax, M., Causse, M. & Bard, P.-Y. Ground motion prediction in Beirut: a multi-step procedure coupling empirical Green's functions, ground motion prediction equations and instrumental transfer functions. *Bull. Earthq. Eng.* **14**.

28. Garces, M. A. On infrasound standards, part 1 time, frequency, and energy scaling. *Inframatics* **2**, 13–35 (2013).

29. Whitaker, R. W., Sondoval, T. & Mutschlecner, J. P. Recent infrasound analysis. In *Proceedings of the 25th Seismic Research Review-Nuclear Explosion Monitoring: Building the Knowledge Base*, 646–654 (Natl. Nucl. Security Admin. Washington, DC, 2003).

30. Vergoz, J., Le Pichon, A. & Millet, C. *Infrasound Monitoring for Atmospheric Studies*, chap. The Antares Explosion Observed by the USArray: An Unprecedented Collection of Infrasound Phases Recorded from the Same Event, 349–386 (Springer, Dordrecht, 2019).

31. Pilger, C. *et al.* The European Infrasound Bulletin. *Pure Appl. Geophys.* **175**, 3619–3638, DOI: 10.1007/s00024-018-1900-3 (2018).

32. Drob, D. P. *et al.* An update to the Horizontal Wind Model (HWM): The quiet time thermosphere. *Earth Space Sci.* **2**, 301–319, DOI: 10.1002/2014EA000089 (2015).

33. Prats-Iraola, P., Scheiber, R., Marotti, L., Wollstadt, S. & Reigber, A. Tops interferometry with terrasar-x. *IEEE Transactions on Geosci. Remote. Sens.* **50**, 3179–3188 (2012).

34. Baran, I., Stewart, M. P., Kampes, B. M., Perski, Z. & Lilly, P. A modification to the goldstein radar interferogram filter. *IEEE Transactions on Geosci. Remote. Sens.* **41**, 2114–2118 (2003).

Author contributions statement

Authors contributions to this study, including data analysis and interpretation, preparation of the figures and results, and writing, are as follows: Seismology and Seismoacoustics (PG, FS, AS, LC), Infrasound (PH, LC, CP), Satellite Imaging (AS, PG, AK, HS). All authors have read, agreed, and participated to the published version of the manuscript.

Competing interests

The authors declare no competing interests.

Data availability

Data from regional seismometers are available via FDSN services from GEOFON and IRIS. Data from global IMS infrasound arrays are available to National Data Centers of the CTBT and to others upon request through the virtual Data Exploitation Center (vDEC) of the IDC at `https://www.ctbto.org/specials/vdec`. Contains modified Copernicus Sentinel data 2020. SAR images used are openly available from the Copernicus Open Access Hub at `https://scihub.copernicus.eu`. ECMWF products, including the atmospheric model analysis, being no longer valid for forecasting are made available via `https://www.ecmwf.int/en/forecasts/dataset` (last accessed 21 Aug 2020) under CC-BY 4.0 License.